Dynamics of water condensation on a switchable surface originated from molecular orientations

Chia-Ming Chang [1,*] Yi-Hsin Lin [1,†] and Victor Reshetnyak [2]
[1]*Department of Photonics, College of Electrical and Computer Engineering, National Yang Ming Chiao Tung University, Hsinchu 30010, Taiwan*
[2]*Theoretical Physics Department, Taras Shevchenko National University of Kyiv, Kyiv 01601, Ukraine*

(Received 2 December 2020; accepted 18 August 2021; published 7 September 2021)

In heat transfer systems, how water condenses on the surface is critical to the energy efficiency of the system. With fixed surface wettability, hydrophilic surfaces enhance the nucleation rate but result in filmwise condensation due to pinning effect, which impedes the heat transfer between water vapor and surface during droplet growth. A hydrophilic surface with high drop mobility is realized with static tailored wettability surfaces, while tunable surfaces have potential in more comprehensive manipulation in condensation with different scale in time and scale. However, the mechanism has rarely been investigated and elucidated. In this paper, we investigate water condensation on a tunable surface originated from surface tension distribution control. The surface tension distribution under applied electric field is modeled and tested. We demonstrate that the surface tension manipulated by liquid crystal orientation alters the nucleation site density. Also, the periodic surface tension distribution aligns condensed water drops and decelerates the radius growth of droplets. The mechanism of active water condensation manipulation can be further applied to other tunable surfaces for various applications such as atmospheric water generator, heat transfer systems, and desalination systems.

DOI: 10.1103/PhysRevE.104.034701

I. INTRODUCTION

Water scarcity is the lack of a sufficient available fresh water resource to meet water demand due to climate change, population growth, and industrial development. It has been a worldwide issue requiring an urgent solution [1]. Water scarcity is mitigated by water harvesting, which is the process of withdrawing fresh water from natural water circulation. Among various water harvesting methods, atmospheric water harvesting (AWH) causes less environmental impact and consumes less energy [2]. AWH employs water condensation on surfaces, which is a process of water transformation from vapor into liquid adhered to a solid surface. During condensation, water molecules undergo a series of thermodynamic and capillary processes including nucleation, intrinsic growth, coalescence, and transportation [3–5]. Water condensation is also the key process in heat transfer systems such as a heat exchanger and desalination [6–8]. Considering the energy efficiency of these systems, the most critical challenge is the conundrum between applying hydrophilic and hydrophobic surfaces for water condensation. In general, hydrophilic surfaces are more adhesive to water molecules and nucleate more water clusters [3,4]. However, water on hydrophilic surfaces is usually pinned with low mobility of contact lines. The pinned contact lines eventually result in filmwise condensation in which the surface is covered with water film. Since water has low thermal conductivity, the heat transfer from vapor water to the surface is insulated and the energy efficiency of the system is decreased. To avoid such a situation, the water drop needs to be removed or transported, which is favored by dropwise condensation on hydrophobic surfaces [9–13]. Dropwise condensation exhibits six to ten times higher heat transfer rate than filmwise condensation [14,15]. Nevertheless, since hydrophobic surfaces possess high critical free energy which is required to be overcome during heterogeneous nucleation [3,4], the nucleation rate is limited. The conflict between hydrophilic surfaces for enhancing the nucleation rate with a hydrophobic property for improving the heat transfer rate has driven vast research attention in the past decade. Cha *et al.* investigated the condensation type of several surfaces and showed that achieving dropwise condensation on hydrophilic surfaces is still challenging [16].

Learning from nature, several surfaces are developed to overcome the conflict in condensation. Hybrid surfaces mimic the Namib desert beetles with hydrophilic regions distributed on hydrophobic surface. The water is captured by the hydrophilic area and transported by the hydrophobic area [17,18]. The anisotropic microstructured surface imitates the skin of a lizard or a rice leaf. The microchannels induce a capillary effect that directionally transports condensed water [19–21]. A hydrophilic rough surface usually pins the water with a Wenzel contact state, in which the water fills the microscaled cavities. Inspired by nepenthes pitcher plants, slippery lubricant-infused porous surfaces (SLIPSs) enhance the mobility of water in the hydrophilic Wenzel state [22–24]. Also, conical shape and asymmetric roughness on cactus spines and spider silks provide a gradient in surface tension [25,26]. The imbalanced surface tension induces unidirectional drop transportation. Park and co-workers suggested solving the paradox in water condensation by integrating the features of hybrid surface, conical shape, and SLIPS [27]. Concluded from the above-mentioned literature,

*mikechang.eo02g@g2.nctu.edu.tw
†yilin@nycu.edu.tw

an ideal surface for water condensation should be hydrophilic, slippery, and be able to actively drive directional drop transportation [28,29]. A heterogeneous hydrophilic surface with low contact angle hysteresis and actively tunable wettability has high potential in fulfilling the requirements. An actively tunable wettability surface is typically achieved with a chemical coating that is sensitive to heat, light, ions, or *pH* [30]. Tunable surfaces with heat, ions, and *pH* are not suitable for water condensation since the stimuli affect or originate from the liquid phase. Light driven tunable surfaces have long reaction time, low capillary force, and pinning effects that hinder the development in water condensation [31]. Recently, electrowetting on dielectric shows the ability to actively control the condensation process [32,33], though the effect is driven by electrostatic energy distribution generated by electrodes and affects the drops only when they grow into size of electrodes. Since water condensation involves water drops from molecular to millimeter scale, tunable wettability induced by molecular properties provides comprehensive control to the whole process.

Water condensation starts with nucleation. Water molecules in air impact the surface, mass transfer, and group up into clusters. According to classical nucleation theory, nucleation is the result of energy transferring between water and solid surface including Gibbs free energy and surface tension [3,4]. The nucleation rate, defined as the number of new nuclei formed on a unit area of surface per second, is affected by hydrophobicity and nucleation site density of the surface [14,34]. After nucleation, stable clusters grow via direct condensation and coalescence as condensation proceeds from atomistic scale to microscale. At first, drops grow by direct accommodation of water molecules in air [35]. The volume increases linearly with time, and the count remains constant. As drops grow larger and touch other drops at their perimeter, they coalesce and create an elongated composite drop. If the surface tension overcomes the pinning of contact line, the contact line recedes and the composite drop becomes circular in shape [13]. Otherwise, the drops remain in irregular shape and become filmwise eventually. A surface with low contact angle hysteresis (CAH) has lower resistance to the dynamics of a contact line, which promotes dropwise condensation [16]. Although coalescence raises the drop radius without increasing the total drop volume, it helps water harvesting via decreasing the area occupied by the initial drops and leaving spaces for further expansion of the drops. It is clear that controlling the timing, rate, and period of coalescence is essential to improve dropwise condensation efficiency.

The above-mentioned challenges have driven us to investigate the condensation process on an active wettability tunable surface. In this research, dropwise condensation is observed on a rough, chemically heterogeneous, and hydrophilic surface made of hydrophobicity switchable interface with nematic liquid crystal (LC) film (Hsin film). The tunability of wetting properties is provided by the orientation of liquid crystal with different free energy of the functional group [36,37]. We investigated the process of water condensation on an electrically tunable wettability surface. The nucleation rate is enhanced with more nucleation sites on Hsin film compared to a smooth glass surface. With the interdigitated electrode design, one dimensional periodic surface tension is distributed on the surface of Hsin film when voltage is applied. The surface tension distribution generated by LC orientation regulated the position of condensed drops, leading to suppression of coalescence during drop growth. After the drops grow larger than electrode gaps, the alignment of drops vanished, and the coalescence recovered. It is shown that actively controlled water condensation is achieved by wettability tunable surface using liquid crystals.

II. METHODOLOGY

The structure of the sample comprises a glass substrate and a Hsin film as illustrated in Fig. 1(a). The bottom substrate was coated with indium tin oxide (ITO), which was etched into two interdigitated chevron electrode patterns. The width and gap of electrodes were 4 and 14 μm respectively. The corner angle of the electrodes was 150°. The two chevron electrodes were connected with two electrode pads respectively for further wiring to input voltage. Before fabricating the sample, the room temperature and the relative humidity were lowered to 18 °C and 45%. To fabricate Hsin film on the ITO substrate, another top substrate was coated with polyimide (Innolux, PI-7492) and mechanically buffed along the y direction. It was then assembled on the top of the bottom substrate to build up an empty cell. The Hsin-film mixture was mixed with nematic LC (Merck, E7), liquid crystalline monomer 4-(3-Acryloyloxypropyloxy)-benzoesure 2-methyl-1, 4-phenylester (Merck, RM247) and photoinitiator 1-Hydroxycyclohexyl phenyl ketone (Ciba, Irgacure 184) at a ratio of 69:30:1 wt %. The empty cell was filled with the mixture under a temperature of 90 °C. After the filling, the temperature was gradually decreased to $T_{\text{curing}} = 70\,^{\circ}\text{C}$. The cell was then exposed to UV light with intensity of $3\,\text{mW/cm}^2$ for 1 h. Due to the photoinitiator, the double bonds at the end of liquid crystalline monomers were broken by UV light and formed cross links between the monomers. The reaction resulted in polymerization and phase separation of the mixture. With a thermal-releasing process, the top substrate was removed, and a solidified Hsin film was left on the substrate with ITO electrodes. To tune the wettability of Hsin film, the electrodes are connected to power supply with 1-kHz squared wave AC voltage [36,37].

The surface morphology is obtained by scanning electron microscope (SEM) (JEOL, JSM-7401F) and atomic force microscope (AFM) (FSM-Precision, Nanoview1000) (See Appendix A for detailed measurement procedures). To characterize wettability of electrically tunable Hsin-film surface, the contact angles, advancing angles, and receding angles were measured with a contact angle goniometer system (First Ten Angstrom, FTA1000). During contact angle measurements, a 3-μL deionized water sessile drop (3.2 mm in diameter) was placed on Hsin film. A charge-coupled device (CCD) camera (JAI CV-M30) with telecentric lens was used to capture images of the drop from the side view to obtain the contact angle. In advancing and receding angle measurements, deionized water was added or extracted from a drop on top of Hsin film by a glass syringe. The contact line of the drop then advanced or receded. The whole process was also recorded by CCD camera. The images and videos were also analyzed

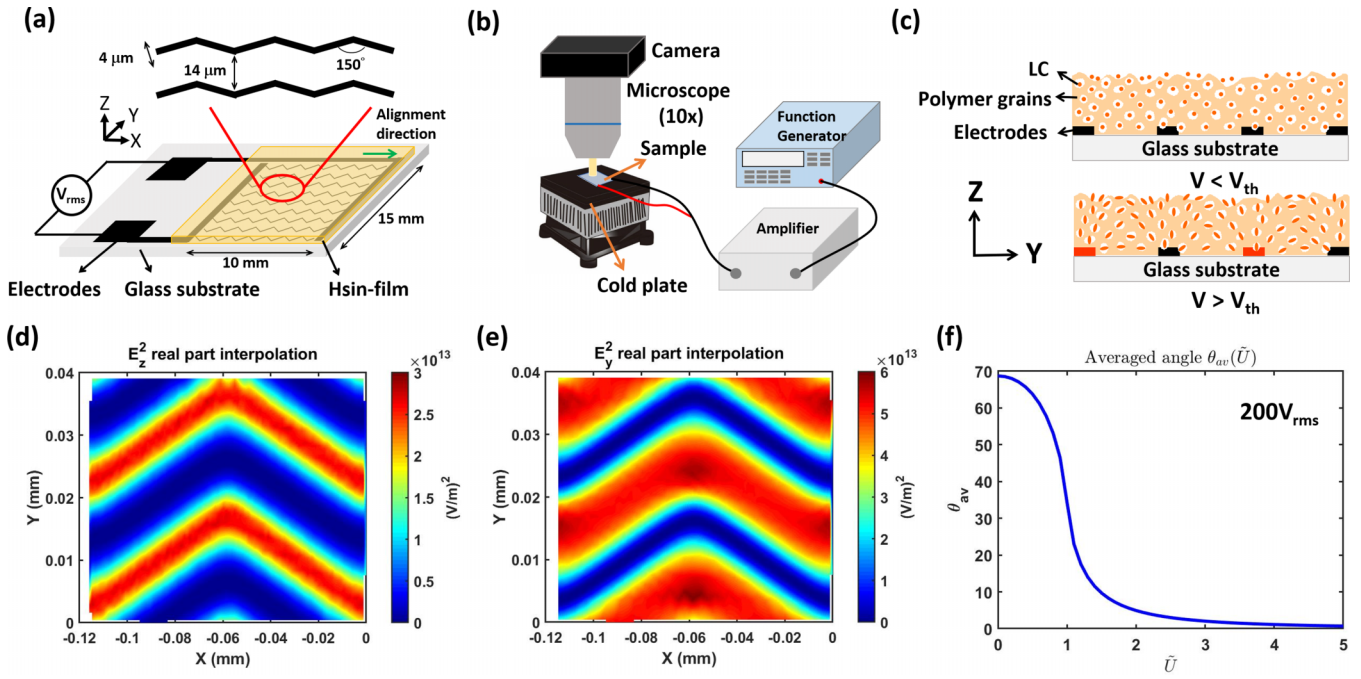

FIG. 1. (a) The structure of a Hsin-film sample on a glass coated with a pair of ITO electrodes. (b) Experimental setup for observing water condensation process on Hsin film with applied voltage. (c) Liquid crystal orientation in polymer under applied voltage lower and higher than threshold voltage. (d) Electric field E_z component dominates in the area above the electrodes. (e) Electric field E_y component dominates in the area between the electrodes. (f) Average value of LC director polar angle with respect to nondimensional applied voltage.

through software (First Ten Angstroms, FTA 32) to obtain dynamic contact angles and other information related to the drop shape under different applied voltages.

We observed the water condensation process through a microscope viewing from the top of the sample [Fig. 1(b)]. The experimental setup involved a temperature tunable cold stage (Advanced Thermoelectric, TCP 50), a microscope with a 10× objective lens (Olympus, U-TR30-2), a camera (Canon, EOS 760D) attached to the microscope, and a power supply with amplifier for tuning of the Hsin-film surface. The temperature and relative humidity of the room was kept at 26 ± 1 °C and 52.5 ± 2.5%, resulting in a dew point of 16 °C. The cold plate was maintained at a surface temperature of 10 ± 0.4 °C throughout the experiment (monitored by a thermocouple and thermometer). At first, the wettability of Hsin film was switched by applying voltage. Second, we started the camera to capture images sequentially. Then the test sample was placed on top of the cold stage. The condensation process was observed for 180 s. The same process was repeated for all the surface conditions with different applied voltages. The experiments were performed in an air-conditioned room. The environmental condition near the sample was monitored (see Appendix B for detailed environmental conditions). Also, the experiment was repeated three times with carefully controlled room temperature and humidity.

III. RESULT

A. Surface properties

The surface of Hsin film is built with porous polymer grains filled with liquid crystal molecules. The LC domains in the SEM image are analyzed with IMAGEJ software by setting proper gray scale threshold and applying particle analysis function. The characteristic domain size was 255 nm on average; the domains occupied 31% of the total surface area. Obtained from AFM scanning, the RMS roughness of the Hsin-film surface was 7.8 nm (please see Appendix A for the surface morphology characterization). With the characteristic surface profile of Hsin film, the effective surface tension at the Hsin-film interface with air is given by [38,39]

$$\gamma_{\text{eff}} = f(\gamma_{\parallel} + \gamma_a \cos^2\langle\theta(U)\rangle) + (1-f)\gamma_{\text{pol}}, \qquad (1)$$

where $\langle\theta(U)\rangle = \int_0^D \theta(U,x)dx$ is the LC director angle averaged over the characteristic size of the area occupied by LC molecules in Hsin film. $\gamma_{\text{pol}} = 30.9\,\text{mJ/m}^2$, $\gamma_{//} = 40\,\text{mJ/m}^2$, and $\gamma_{\perp} = 91.6\,\text{mJ/m}^2$ are the surface tension of polymer, planar LC, and homeotropic LC. $\gamma_a = \gamma_{\perp} - \gamma_{//} = 51.6\,\text{mJ/m}^2$. $f = 0.31$ is the surface fraction of LC obtained by SEM images. To get some insight on the electric field effect on the effective surface tension we adopt the following model: The photopolymerization process results in the LC confined to small domains bounded by polymer walls, the characteristic size of domains is $D = 255\,\text{nm}$. Under an externally applied electric field, the LC director is reoriented inside each domain. The LC orientation within domain is initially given by the domain polymer wall's averaged orientation; we denote this orientation by the angle θ_0 (in some sense it is the easy axis direction for the LC director inside domain). The angle θ_0 is different in different LC filled domains which depends on the photopolymerization process. The distribution function for the angle θ_0 in different domains is given by $p(\theta_0)$. The electrostatic interaction of the LC director $\vec{n}$ with the electric

field $\tilde{E}$ is described by the energy density

$$F_E = -\tfrac{1}{2}\varepsilon_0\varepsilon_a(\vec{n}\cdot\vec{E})^2, \tag{2}$$

where ε_a is the LC dielectric anisotropy at the frequency of the applied electric field and $\vec{n}$ is the LC director averaged over the domain volume. The polymer wall–LC interface provides the LC director anchoring. We assume that an individual domain wall provides easy axis $\vec{L}_0$ for LC orientation within a given domain. There is an elastic energy associated with rotation about this axis, F_{el}. We suppose that the LC interaction with the polymer domain walls has a simple phenomenological form

$$F_{el} = -WS(\vec{n}\cdot\vec{L}_0)^2, \tag{3}$$

where the parameter $W > 0$ characterizes the magnitude of the interaction, and S is the surface area of the domain. We further assume that the LC interaction with the polymer matrix is proportional to S because it occurs at the domain boundary. Therefore, it is likely to scale with the domain surface area.

We neglect the LC director reorientation effect on the electric field spatial profile and find the electric field produced by chevronlike electrodes by assuming the effective dielectric constant of Hsin film to be 6.46. Then the total energy to be minimized to find the LC director orientation under the applied electric field reads

$$F = F_{el} + F_S = -\tfrac{1}{2}\varepsilon_0\varepsilon_a V(\vec{n}\cdot\vec{E})^2 - WS(\vec{n}\cdot\vec{L}_0)^2. \tag{4}$$

The averaged total energy over the azimuthal angle in the Hsin-film area where the E_z component is the highest compared to other electric field components can be written as

$$\begin{aligned} F &= -\int_0^{\pi/2} p_0(\theta_0)\left(\frac{1}{2}V\varepsilon_0\varepsilon_a E_z^2\cos^2\theta - WS\sin^2(\theta-\theta_0)\right)d\theta_0 \\ &= -WS\int_0^{\pi/2} p_0(\theta_0)\left(\frac{1}{2}\tilde{U}^2\cos^2\theta - \sin^2(\theta-\theta_0)\right)d\theta_0. \end{aligned} \tag{5}$$

V is the domain volume and $\tilde{U}^2 = \frac{V\varepsilon_0\varepsilon_a E_z^2}{WS}$ is the dimensionless parameter characterizing the applied voltage in the Hsin-film area where the E_z component dominates in the total electric field. In the Hsin-film area where the E_y component dominates the dimensionless parameter should be replaced by $\tilde{U}^2 = \frac{V\varepsilon_0\varepsilon_a E_y^2}{WS}$. The square of electric field E_z^2 and E_y^2 spatial profile are simulated with modeling software COMSOL and the results are shown in Figs. 1(d) and 1(e). It is seen that the electric field y component dominates in the areas in between the electrodes and reorients the LC inside pores in polymer matrix parallel to the film surface (planar LC alignment). In the area above the electrodes the electric field z component dominates forcing the LC director to reorient into the homeotropic state.

We schematically show how the electric field influences the surface tension distribution via liquid crystal orientation in Fig. 1(c). When no voltage is applied, the liquid crystal molecules at the surface of LCPCF are aligned approximately in the y direction. The biphenyl group of LC molecules is exposed to air that results in homogeneous low surface tension. When voltage higher than threshold is applied, the electric field drives the LC molecule to tilt as shown in the bottom graph in Fig. 1(c). More of the polar cyano group is revealed to air, which makes the surface more hydrophilic with higher surface tension.

The minimization of the energy [Eq. (5)] results in the following equation for the LC director:

$$\theta(\theta_0,\tilde{U}) = \tan^{-1}\left(\frac{\sin(2\theta_0)}{\tilde{U}^2+\cos 2\theta_0 + (\tilde{U}^4+2\tilde{U}^2\cos 2\theta_0+1)^{1/2}}\right). \tag{6}$$

In Fig. 1(f), we theoretically show the averaged value of the LC director angle $\theta_{av}(\tilde{U}) = \langle\theta(\theta_0,\tilde{U})\rangle_{\theta_0}$ versus nondimensional electric potential. The averaging is done over 100 uniformly distributed random values of the initial angle θ_0. From Fig. 1(f) it is seen that the director reorientation has thresholdlike behavior with the nondimensional threshold voltage $\tilde{U}_{\rm th} \approx 0.5$. From the measurement results of contact angle, advancing, and receding angle (Fig. S3 in the Supplemental Material [40]), we observed that the threshold voltage required to change the orientation of LC, in fact, to change the contact angle, is $V_{\rm th} \sim 60\,V_{\rm rms}$.

Now we are ready to calculate the effective surface tension [Eq. (1)] subject to knowing the distribution function $p(\theta_0)$. We shall assume that the angle θ_0 takes values between 0 and $\pi/2$, and the distribution function $p(\theta_0)$ within domains occupied by LC takes the form $p(\theta_0) = 0.5 + 0.5P$, where P is the uniformly distributed random number within [0,1]. Figures 2(a) and 2(b) show the effective surface tension at 0 and 200 $V_{\rm rms}$ of a 1-kHz AC electric field in the case of weak anchoring with anchoring energy $W = 10^{-5}\,\mathrm{J/m^2}$. The surface tension in the Hsin film area above the electrodes rises to 50 $\mathrm{mJ/m^2}$ when 200 $V_{\rm rms}$ is applied.

The contact angle was tuned from 88° to 74° when 200 $V_{\rm rms}$ was applied. Contact angle hysteresis (CAH) is defined as the difference between advancing and receding angle. Hsin film demonstrated CAH of 5° when $V < V_{\rm th}$, and the CAH rose to 8.5° as voltage increased to 140 $V_{\rm rms}$. After that, the CAH dropped to 5° when the voltage was 200 $V_{\rm rms}$. The CAH of water drop on Hsin film was lower than 10° throughout the operating voltages, indicating the surface is slippery and assists in the ease of droplet movement. From the contact angle and CAH, the work of adhesion and surface tension of Hsin-film surface can be determined as a function of voltage [41]. The resulting work of adhesion and surface tension is shown as blue circles and red squares in Fig. 2(c). The work of adhesion varies from 75 to 93 $\mathrm{mJ/m^2}$. The surface tension varies from 36 to 45 $\mathrm{mJ/m^2}$ with applied voltage. From Fig. 2(c), we observed that the threshold for surface tension and adhesion is similar to that of CA, which is around 60 $V_{\rm rms}$.

From the SEM images, AFM images and wettability measurements, we obtained that Hsin-film surface is highly heterogeneous and slightly rough. The contact angle is lower than 90°, indicating that the surface is hydrophilic and the water drop is in the Wenzel state among the applied voltage range. Despite being in the sticky Wenzel state, the low CAH shows high drop mobility. We expected dropwise condensation on the hydrophilic surface of Hsin film, which is rarely achieved on untreated surfaces. Furthermore, the condensed drops are in nano- to micrometer scale. Thus, the wettability distribution caused by the microscale electrode pattern as well

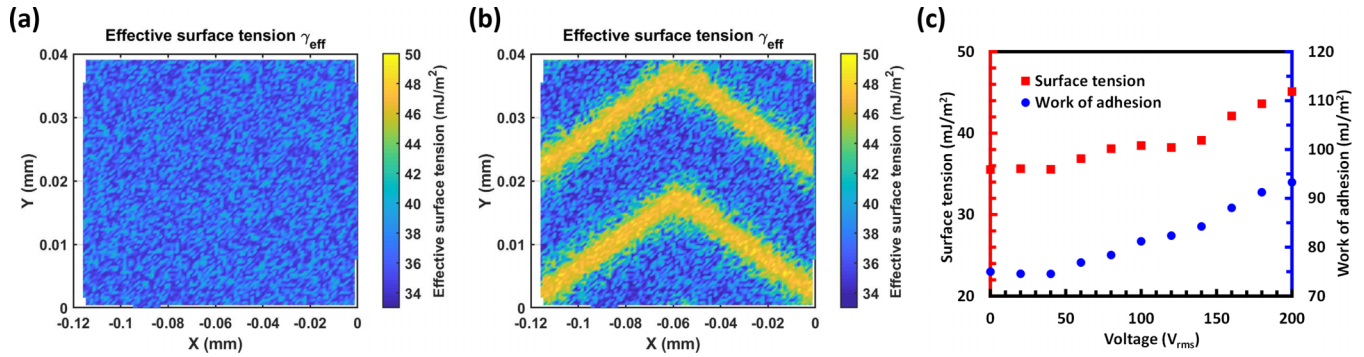

FIG. 2. Simulation result of effective surface tension under (a) $0\,V_{\rm rms}$ and (b) $200\,V_{\rm rms}$. (c) Surface tension (red dots) and work of adhesion (blue dots) of Hsin film as a function of voltage.

as nanoscale LC domains must be considered. Due to the periodic electrode design, the surface tension distribution of LC molecules on the surface is also periodic. According to the simulation result [Figs. 1(d) and 1(e)], the surface tension right above the electrode is tuned from 36.6 to 47 mJ/m^2 with a LC molecule tilt angle of ∼60.5° when applied with $200\,V_{\rm rms}$. It is estimated to be up to 85 mJ/m^2 if the average tilt angle of LC molecules is 90° [37]. As a result, the average surface tension over the periodic distribution is tuned from 36.6 to 43 mJ/m^2.

B. Water condensation

The microscopic top view of condensed water droplets on the chemically heterogeneous Hsin-film surface is shown in Fig. 3 with region of interest in size of $0.59 \times 0.36 = 0.2124\,\text{mm}^2$ (please see videos in [40]). The applied voltages shown in the figures are $0\,V_{\rm rms}$ (lower than threshold), $80\,V_{\rm rms}$ (activated), and $140\,V_{\rm rms}$ (higher voltage). Comparing Hsin-film surface with glass surface [Figs. 3(a) and 3(b)], it is seen that the shape of drops on Hsin film was spherical cap (dropwise condensation) even though Hsin film is hydrophilic with a contact angle lower than 90°. In contrast, the shape of the drops on glass substrate was deformed into irregular shape when they grew larger with coalescence. This was due to the higher CAH (∼30°) and more hydrophilicity (contact angle = 45°) of glass that prevented the contact line from retraction after drop coalescence. Furthermore, the drop count on the Hsin-film surface was more than that on glass substrate in a 5-s time frame. This is due to the heterogeneity and roughness of Hsin film consisting of liquid crystal domains and polymer grains which served as nucleation sites. When the applied voltage is higher than threshold voltage ($80\,V_{\rm rms}$ for example), we observed the condensed drop aligning between electrodes [Figs. 3(c) and 3(d)]. The alignment effect further increased with higher applied voltage. We also

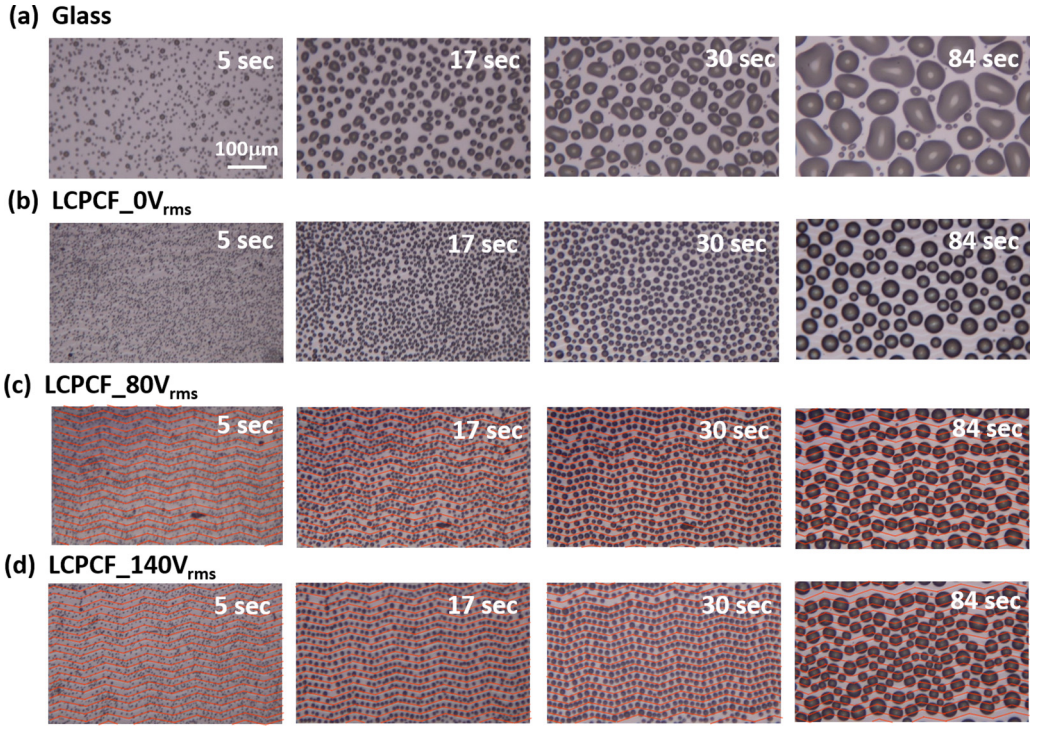

FIG. 3. Images of water drops condensed on (a) glass and Hsin film with applied voltage of (b) $0\,V_{\rm rms}$ (c) $80\,V_{\rm rms}$, and (d) $140\,V_{\rm rms}$ at the time 5, 17, 30, and 84 s after the substrates contact with the cold plate. The electrodes geometry under Hsin film is indicated by the red lines.

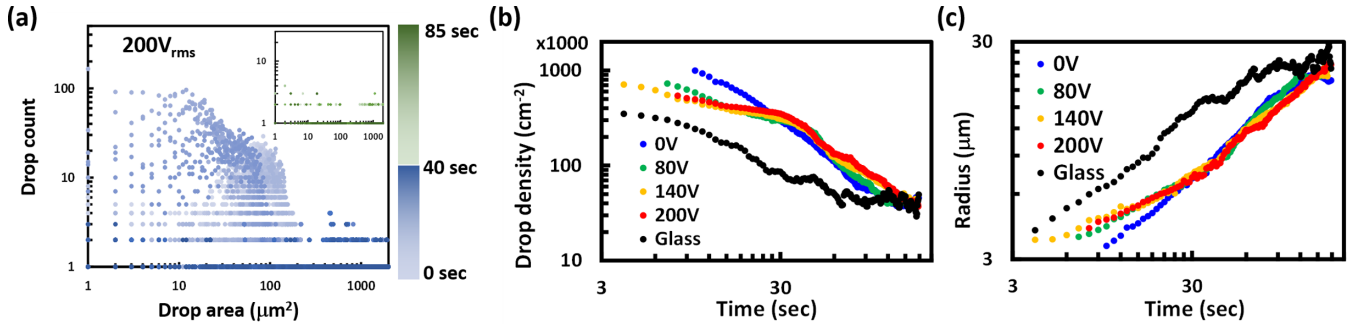

FIG. 4. (a) Histograms of the condensed water drops amount with respect to drop size on Hsin film with applied voltage of 200 V_{rms}. The period of 0–40 s is gradually colored in blue, and the period of 40–85 s is gradually colored in green in the subplot. Logarithmic plot of (b) water drop density and (c) average drop radius with respect to time on Hsin film with different applied voltage and glass.

discovered that the drops at the early stage (<5 s) is randomly distributed regardless of applied voltage. Thus, the alignment of the drop was the result of coalescence on periodic surface tension distribution (∼5–40 s). In the later stage of condensation (>40 *s*), the droplet grew large enough to cover the electrode region and the coalescence is mostly by crossing the electrodes. The newly formed droplet grows wider between the electrodes becoming less elliptical and the alignment of the drop is less obvious. Also, in the freely exposed region, the new cycle of nucleation starts and follows a similar growth process. The images were cropped, binarized, and analyzed by software IMAGEJ (see Appendix C for detailed image processing and analysis). The drop count with respect to the drop area was converted into drop size distribution to show the evolution of water drops on the surfaces. Figure 4(a) shows the evolution of condensed water drop size distribution on Hsin film applied with 200 V_{rms} (see Appendix D for detailed drop size distribution). Typically, the drop size distribution during water condensation follows the self-similar evolution and shows bimodal distribution [42,43]. However, the bimodal distribution was not significant in our experiment result. We postulated that the surface of Hsin film has very low contact angle hysteresis no matter whether voltage is applied. As a result, the period for the small drops to grow by direct phase change (intrinsic growth) is short (less than 2 s). The linear varying distribution transformed into bell-shaped distribution rapidly and it causes the two peaks (from drops formed earlier and later) in the bimodal distribution to become so close that it shows only one wide bell-shaped distribution as they grow mainly by coalescence. Though the bimodal distribution is not significant, we still can observe new cycles of condensation in the images. As the old drops grow bigger, smaller drops condense and coalesce. When voltage is applied, the coalescence is inhibited and causes the two bell-shaped distributions to separate more.

IV. DISCUSSION

A. Drop alignment

When Hsin film is subject to the applied voltage with the magnitude higher than threshold, the water drops are aligned in the area between the electrodes. However, the simulation result shows that the area between electrodes has lower surface tension compared to the area on the electrodes. There are studies on LC orientation at water-5CB interface and they show that the LC (5CB) is aligned parallel to the interface with water [37,44]. This means that the areas of Hsin film where the water condensation starts and where the water droplets are in the later stage should have planar LC alignment. The modeling of effective surface tension is done for the air-LC interface. For air-LC interface, the surface tension is higher for homeotropic orientation. At the water-LC interface the surface tension is higher for planar orientation. We know this because the LC is planarly oriented at the interface with water. Therefore, despite that we don't know the absolute values of surface tension for the water-LC interface when LC is in a homeotropic and planar state, we can say that the effective surface tension anisotropy of Hsin film at the interface with water will be opposite the one shown in the modeling for the Hsin-film interface with air. Namely, the effective surface tension for air and Hsin film is raised on top of the electrodes, but the effective surface tension for water and Hsin film is lowered when voltage is applied. According to Young's equation and the contact angle we obtained, the surface tension for the water–Hsin-film interface is lowered from 33.5 to 25 mJ/m^2 with 200 V_{rms} of applied voltage.

Besides, the directional transportation of droplets not only depends on the surface tension gradient but also depends on the contact angle hysteresis caused by heterogeneity [45].With a micrometer-sized droplet on Hsin film, the heterogeneity generated by the polymer-LC composite surface should be considered. According to the simulation result in Fig. 2(b), it seems that the surface tension is higher on top of the electrodes. However, the heterogeneity of surface tension at the area between electrodes is higher (ranging 34–42 mJ/m^2) while it is more homogeneous on top of the electrodes (∼50 mJ/m2). The heterogeneity enhances the wettability and hysteresis that attracts the microsized droplets to align between the electrodes. Unfortunately, we are not able to quantitively measure the wettability on such a tiny area. In Fig. 2(c), the surface tension is measured with a millimeter-sized drop, which "feels" the surface tension averaged over the pores and the electrodes. In conclusion, the wettability of a water drop on Hsin film should consider the size of the drop with respect to the configuration of electrodes as well as the LC-pore composition.

B. Drop density and radius evolution during growth

A typical drop density evolution of dropwise condensation decreases according to a power law [28]. On glass substrate, the decaying curve is fluctuated since the condensation is not fully dropwise as shown in Fig. 3(a). The decay saturated when $t \sim 70$ s. On Hsin film with applied voltage lower than threshold, the decay curve is smooth and saturated when $t \sim 84$ sec (the time frame shown in fourth column of Fig. 3). As the applied voltage exceeded the threshold value, a flat terrace formed in the period of 17–30 s (the time frames shown in second and third columns of Fig. 3). Higher applied voltage results in a flatter terrace and occurs earlier. After the flattened terrace (30–180 s), the drop density decayed again with power law (see Appendix E for more discussion on nucleation density).

The growth of drops is an interplay between intrinsic growth and coalescence. According to the Rogers model, the drop density decays exponentially with coalescence [46,47]:

$$N(t) \sim t^{\mu_d} N_0, \tag{7}$$

where N_0 is the initial drop density and the exponent μ_d characterizes how frequently the drops coalesce. During intrinsic growth, the drops grow individually and lead to static drop count ($\mu_{di} = 0$). With coalescence assisting the growth, the number of drops decreases with the exponent $\mu_{dc} = -3/2$. Figure 4(b) shows the drop count density decay in a logarithmic plot. The slopes of the curve indicate the exponents μ_d of each condition in different growth stages. As the applied voltage exceeded the threshold value, the curves exhibited flattening with transition time at ∼17 s. When the applied voltage is in the range 80−200 $V_{\rm rms}$, an extra flat segment from 17 to 30 s emerges. After 30 s, the curves recover the slope as a sample without applied voltage. Moreover, the average drop radius rises during intrinsic growth and coalescence. According to previous research, the average drop radius growth is described as [5,47–49]

$$r \sim t^{\mu_a} r_0, \tag{8}$$

where μ_a is the exponent of average drop radius growth which depends on the mechanism of growth. For initial growth, the drops accumulate a new water molecule with static flux of monomers by mass transfer. Hence, the volume of the drops increases linearly with time. The geometrical relation between drop radius r and volume Ω is

$$r = \left[\frac{3\sin^3\theta}{\pi(1-\cos\theta)^2(2+\cos\theta)}\Omega\right]^{1/3}, \tag{9}$$

where θ is the contact angle. As a result, the radius grows with an exponent of $\mu_{ai} = 1/3$ [5,48]. In coalescence, the radius growth exponent depends on the difference in dimensionality between the drop D_d and surface D_s, which is described as

$$\mu_{ac} = \mu_{ai}\frac{D_d}{D_d - D_s}. \tag{10}$$

Considering that water drops coalesce on a typical two-dimensional surface, D_d is 3 and D_s is 2. As a result, the average radius is linearly proportional to time ($\mu_{\rm ac} = 1$) [5,48]. Figure 4(c) shows the logarithmic plot of drop radius growth on Hsin film and glass. The curve of Hsin film without applied voltage is nearly a straight line, while it broke into a two-step response with the slope of the first step gentler than the second one when applied with a voltage higher than threshold. The curve for glass surface starts with a steeper slope followed by a slope with less inclination. The fluctuation in the later stage is cause by new nuclei which are smaller in size [Fig. 3(a)].

C. Drop density decay rate and radius growth rate

During the condensation, two growth processes occur concurrently. We adopt the exponents of drop count decay and radius growth to indicate how water drops grow. We linearly fit the logarithmic plot [Fig. 4(b)] with the function $\log_{10}(N) = \mu_d \log_{10}(t) + C_d$. The fitting is divided into two or three parts due to the two-step or three-step response. The slopes indicate the exponent μ_d in Eq. (7), and the values are plotted in Fig. 5(a) with respect to applied voltage. $\mu_{\rm d1}$, $\mu_{\rm d2}$, and $\mu_d{}'$ are exponents of the first, second, and extra segment respectively while the dashed lines are the result of glass substrate. On Hsin-film surfaces, the effect of liquid crystal orientation is revealed in the exponent of the first step $\mu_{\rm d1}$. It is −1.2 with voltages less than the threshold voltage. As the voltage exceed the threshold voltage, $\mu_{\rm d1}$ rises to −0.5. This means that as the tilt angle of LC increases with applied voltages, the occurrence of coalescence is reduced, and intrinsic growth starts to dominate. The extra $\mu_{\rm d}{}' \sim -0.3$ shows even higher suppressing of coalescence during 20–40 s. With the highest applied voltage (160–200 $V_{\rm rms}$), $\mu_{\rm d1}$ reaches −0.3 in the whole 0–30-s period. $\mu_{\rm d2}$ is in the later stage when the drops are larger than electrode gaps and not aligned. The growth is mostly assisted by coalescence. The value is −1.4 for all voltage applied, which is similar to what was reported earlier [46].

The change in mean radius with respect to time is plotted in a log plot [Fig. 4(c)] and fits with linear function $\log_{10}(r) = \mu_a \log_{10}(t) + C_a$ [5,14]. r is the average radius of each frame, t is time, and C_a is the fitting constant. The fitting parameter $\mu_{\rm a}$ is the slope of the fitting function; it also represents the exponent of radius growth in Eq. (8). We observed two powers ($\mu_{\rm a1}$ and $\mu_{\rm a2}$) that correspond to the growth rate in early and later stages. As shown in Fig. 5(b), when the voltage is lower than threshold, the exponent starts with $\mu_{\rm a1} \sim 0.6$ and is followed by $\mu_{\rm a2} \sim 0.8$. When applied voltage is increased, $\mu_{\rm a1}$ drops down to ∼0.4 and is also followed by $\mu_{\rm a2} \sim 0.8$. The phenomenon indicates that coalescence is inhibited during the early stage of growth due to the periodic alignment of water drops. $\mu_{\rm a2}$ is the state when drops grow larger and the high thermal resistance offered by the large droplet reduces the adsorption of water molecules [46]. Also, the alignment is diminished since the drop is large compared to the electrode pattern. The drops can move in all directions as on normal surfaces. In this state, drop growth is mostly due to coalescence.

On glass substrate, drops are highly pinned so that coalescence is suppressed. Therefore, $\mu_{\rm d1}$ of glass are higher than −1 [red dashed line in Fig. 5(a)]. In the later stage, there are new drops formed in free exposed spaces that compensate for the decay [blue dashed line in Fig. 5(a)]. On the other hand, the value of $\mu_{\rm a1}$ for glass is similar to Hsin film without the effect of LC [red dashed line in Fig. 5(b)]. However, the value

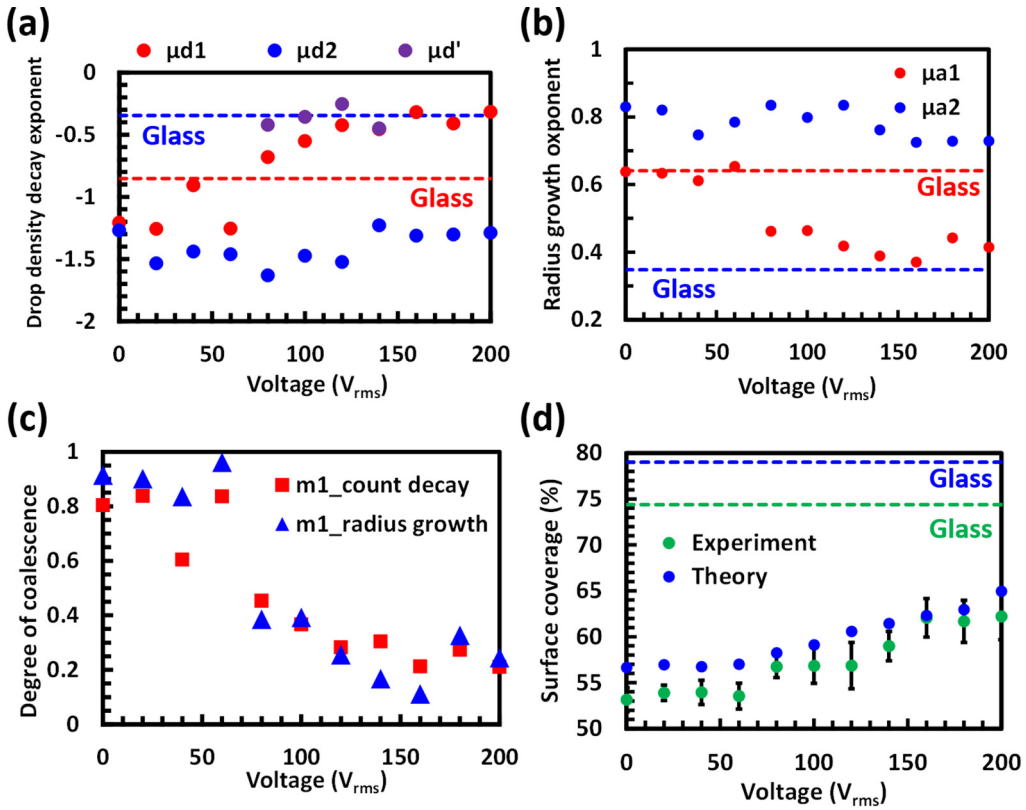

FIG. 5. The exponents of (a) drop density decay and (b) average drop radius growth at different stages as function of applied voltage. (c) Degree of coalescence of the first stage in drop count decay and drop radius growth. (d) Saturated surface coverage as function of applied voltage. Dashed lines are result from glass substrate.

of $\mu_{a2} = 0.35$ for glass surface is much lower than for Hsin film [blue dashed line in Fig. 5(b)]. During this state, the presence of new nucleation causes fluctuation in mean droplet radius [Fig. 3(a)]. The coalescence mostly comes from large drops (first cycle) absorbing tiny ones (second or third cycle), causing a low growth rate in the size of the large drops.

The effect of LC orientation on Hsin-film surfaces is mainly pronounced in the early step (μ_{d1} and μ_{a1}). To interpret how much the growth process depends on coalescence, we propose a conceptual factor m describing the degree of coalescence (DOC). We assumed that all the coalescence has only two drops involved. Factor m represents the possibility of the drops on the surface coalesce with another drop during a certain time interval. For example, $m = 1$ indicates that all the drops coalesce. In contrary, $m = 0$ represents full domination of initial growth and no coalescence happens. For drop count density decay, the exponent is modeled as

$$\mu_d = (1 - 2m)\mu_{di} + m\mu_{dc}. \tag{11}$$

The factor $(1-2m)$ is due to that two drops are involved in a single coalescence process. Since $\mu_{di} = 0$ and $\mu_{dc} = -1.5$ [46], the exponent $\mu_d = -1.5 \times$ m. The same factors should also apply to the exponent of radius growth with the linear relation of

$$\mu_a = (1 - 2m)\mu_{ai} + m\mu_{ac}, \tag{12}$$

where $\mu_{ai} = 1/3$, $\mu_{ac} = 1$, and the exponent $\mu_a = (m + 1)/3$. The resultant DOCs analyzed with the first stage of drop count decay and drop growth are similar [Fig. 5(c)], indicating that the model is applicable. When the applied voltage is higher than threshold (60–140 V_{rms}), the surface tension distribution restricts the drop mobility in between two electrodes, which leads to moderate suppression of coalescence ($m \sim 0.3$). With higher applied voltage (140–200 V_{rms}), the strong pinning by LC molecules almost eliminates coalescence ($m \sim 0.1$), and the growth is primary contributed by initial growth. Since the fact that three or more drops could participate in one coalescence and multiple coalescence of the same drop might occur during the period, the conceptual model can be further modified with more variables.

D. Surface coverage

Surface coverage is the area portion covered by water drops, which plays an important role in heat transfer rate. When the drops nucleate and grow only by intrinsic growth, the maximum surface coverage that can be achieved is ~55% [42,50]. As the drops coalesce, the resultant surface coverage depends on the CA of the surface. The maximum surface coverage that can be achieved is theoretically approximated as $\varepsilon_\infty = 1-0.005\,\theta$ [5,14]. Figure 5(d) shows the experimentally achieved ε_∞ compared with theoretically computed data by contact angle measurement. On all the surfaces we tested, the saturated surface coverage was achieved before 50 s. Since the contact angle of glass surface is lower, ε_∞ is ~74.3%. It is observed that ε_∞ obtained from experimental results for Hsin film closely match the theoretical

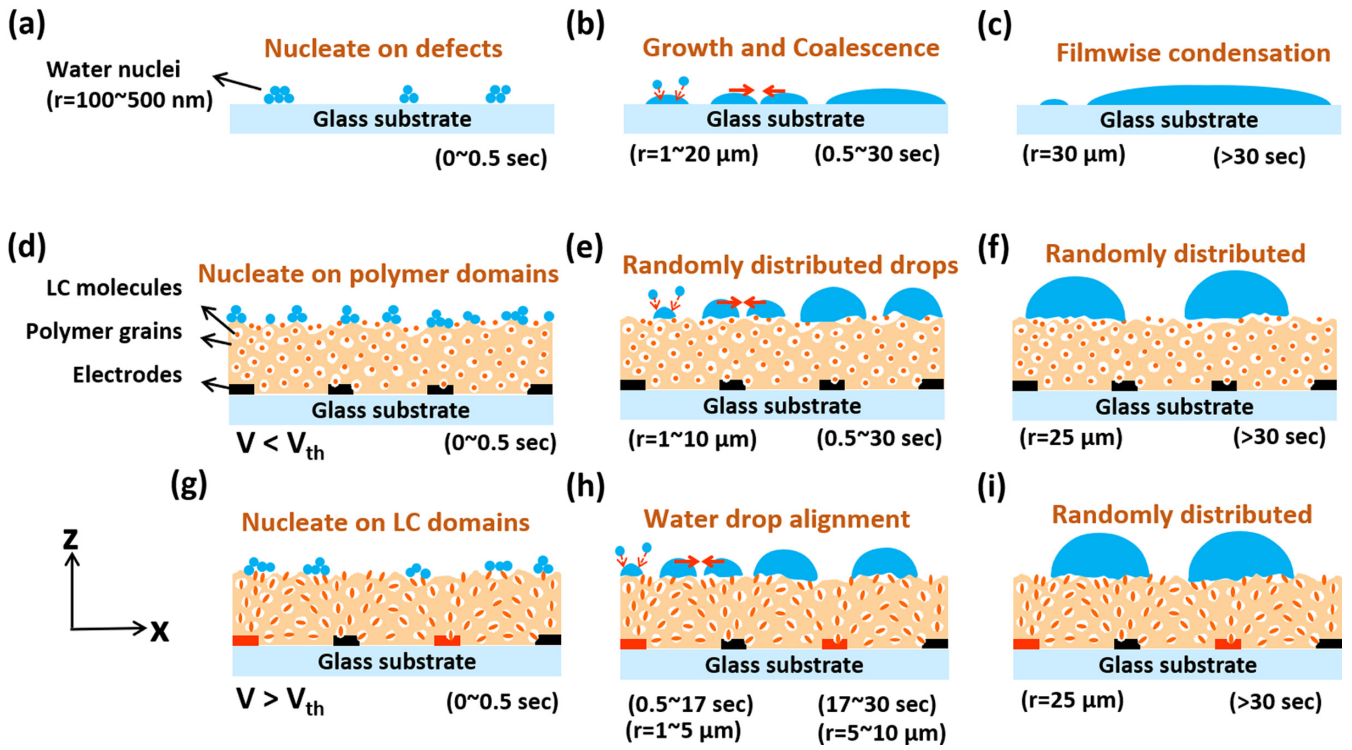

FIG. 6. Water condensation process on (a)–(c) glass substrate, (d)–(f) Hsin-film surface with applied voltage lower than threshold and (g)–(i) higher than threshold. (a), (d), (g) Vapor water nucleate on different nucleation sites. (b), (e), (h) nuclei grow by condensation and coalesce. Water drops aligned at the local minimum of surface tension distribution. (c), (f), (i) Final state of water drops (figures not drawn to scale).

estimation. For glass surface, the large difference may be due to the effect of surface roughness and irregular droplet shape.

E. Condensation on Hsin film

From the observation and analysis, the dynamics of water condensation on glass and Hsin film with and without applied voltage is illustrated in Fig. 6. First, water molecules nucleate on nucleation sites on surfaces. On glass surface, the surface is smooth and homogeneous with fewer defects serving as nucleation sites. The nuclei density is five times less than heterogeneous Hsin-film surfaces [Fig. 6(a)]. On Hsin-film surface without activation, water nuclei formed mostly at exposed polymer grains [Fig. 6(d)] since the surface tension of polymer ($\sim$30.9 mJ/m^2) [37] is higher compared to the phenyl or terphenyl part of liquid crystals ($\sim$29 mJ/m^2) [51]. When Hsin film is activated with voltage higher than threshold, liquid crystal molecules tilt up and expose its cyano part which has a higher surface tension of $\sim$154 mJ/m^2 [37]. The nuclei were likely to form at LC domains [Fig. 6(g)]. Since the LC domains occupied only 31% of the surface, the nuclei were 45% less than that without voltage. This process happened in the period of less than 0.5 s when the condensation starts.

Next, stable nanonuclei accumulate more water molecules and grow larger into microsize. As the drops are large enough to touch each other ($t \sim 3$ s), they coalesce into even larger drops [Fig. 6(b), 6(e), and 6(h)]. On glass surface, since the surface is more hydrophilic, and the contact line is pinned after coalescence, the drops are larger with low contact angle and irregular shape. On Hsin film, the drops remain circular shaped after coalescence, resulting in dropwise condensation. Without activation, the drops are randomly distributed [Fig. 6(g)] while they are aligned at the place where surface tension has local minimum when applied with voltage higher than threshold during $t = 17$–30 s [Fig. 6(h)]. The alignment of drop inhibits coalescence which slows down the growth in drop size.

Finally, when the surface coverage saturated ($t > 30$ s), the filmwise condensation on glass surface results in water patches with new small nuclei at the gaps [Fig. 6(c)]. On Hsin film without activation, circular drops with a radius of 25 μm randomly distributed on the surface with less new nuclei since the tiny nuclei are highly mobile on Hsin film and absorbed easily by large drops [Fig. 6(f)]. Drops on Hsin film with activation are no longer restricted by surface tension pattern and randomly distributed since the drops are larger than the electrode gaps [Fig. 6(i)]. Comparing with the result in electrowetting on dielectric [32], Hsin film provides extra manipulation of nucleation site and surface coverage at the early stage and later stage of condensation since the controlling agent LC domain is in $\sim$100-nm scale. The effect of electrowetting only applies when the drop is approximately the size of the electrode gap. Also, the surface used in electrowetting on dielectric is hydrophobic, which lacks the ability to enhance the water nucleation rate. The whole condensation process took six times longer than Hsin film to reach saturated surface coverage with such low surface tension of the surface. The tunable range in contact angle of Hsin film is less than 20°, causing a limited effect on nuclei density and surface coverage. Further applying LC molecules that contain

functional groups with a larger difference in polarity such as fluoride may improve the surface tension tunability range of Hsin film.

V. CONCLUSION

Dropwise condensation on a heterogeneous hydrophilic surface is realized with Hsin film. Also, we controlled the condensation process with the tunability in wetting properties provided by liquid crystal orientation. The tunability in effective surface tension distribution according to the surface tension of the molecules is modeled and agreed with the experimental results. During condensation, the heterogeneity of Hsin film surface provides more nucleation sites for water nucleation compare to homogeneous glass surface. With applied voltage, the nucleation site is switched from polymer grains to liquid crystal domains. During drop growth, the surface tension distribution influences the process by aligning the drops. When applied voltage is higher than threshold value and water drop size is on the scale similar to the electrode pattern, the orientation distribution of LC molecules causes periodic surface tension layout that confines the location of water drops in between the electrodes. The periodic alignment of water drops restricts and delays the drops to coalesce, which results in a slower growth rate in drop size. We proposed a quantitative factor to describe the degree of coalescence during growth process. We found that Hsin film controls the degree of coalescence by LC orientation. Finally, the saturated surface coverage is enhanced with applied voltage since the average surface tension is raised. According to our result, tunable wettability surfaces actively manipulate the condensation with a different mechanism in each step including nucleation, intrinsic growth, coalescence, and saturation. It should be noted that the properties of the Hsin film are not optimized yet for real applications. In the current study we only show a possibility to electrically tune the surface tension of Hsin film. One may think of stretching the Hsin film to make the pores (and LC inside the pores) to be oriented in one direction, in which case we expect a wider range of the surface tension tuning. The proposed concept can be further applied to other tunable surfaces with various tuning stimuli. Further development on promoting coalescence via switching the surface and actively removing the condensed drops is expected to elevate the efficiency of water harvesting surfaces.

ACKNOWLEDGMENTS

This research was partially supported by Department of Natural Sciences and Sustainable Development in Ministry of Science and Technology, Taiwan under Contracts No. MOST 107-2112-M-009-019-MY3 and No. MOST 110-2112-M-A49-024. The authors express their gratitude to Dr. H.-M. Chen for consultation in the theory and experimental results, and M. Somarapalli and P.-T. Lin for assisting in the experiments, image processing, and data analysis. We are grateful to LCD company Innolux and AUO for the fabrication of glass substrates with patterned ITO and alignment layer.

Y.H.L. conceptualized the work and supervised the project; C.M.C contributed in conducting the experiments, data analysis, and composing the manuscript. V.R. constructed the surface tension model and the simulation. All authors discussed the results and proofread the manuscript.

APPENDIX A: SURFACE MORPHOLOGY

The surface of Hsin film was inspected via scanning electron microscope (SEM) and atomic force microscope (AFM). Before SEM measurement, the LC molecules were removed by soaking the sample with hexane for 24 h and the samples were coated with platinum (15 mA, 150 s). The electronic beams with voltage of 5 kV were injected into the samples to obtain images. From the images in Fig. S1(a) of the Supplemental Material [40], we obtained the morphology of the surface consisting of porous polymer grains. The polymer grains aggregated into networks along with the alignment direction indicated by white arrows in Fig. S1(a) [40]. We analyzed the SEM images with software IMAGEJ. The images undergo the process of crop and background subtraction. The threshold is set by default and results in Fig. S1(b) [40]. By applying particle analysis, we obtained the area ratio of liquid crystal domains as indicated in Fig. S1(b) [40]. The data we used in the main paper are the average of the four results.

In AFM measurements, the LC molecules in Hsin-film samples were deliberately unremoved to preserve original roughness of the surface. The cantilever (Olympus, AC200TS) used in the AFM has a resonance frequency of 150 kHz and spring constant of 9 N/m. The measurements were operated in tapping mode. From the result in Fig. S2 [40], the average RMS roughness is 7.76 nm.

APPENDIX B: ENVIRONMENTAL CONDITION

During the condensation process, the surface temperature of the Hsin film is monitored by placing a surface contact thermometer (Fisher Scientific, dual channel thermometer), on top of the Hsin film surface. Also, during the condensation process for every surface condition, the relative humidity, room temperature, and dew point temperature close to the Hsin film surface is closely monitored (Psychrometer thermometer) and recorded. The room temperature measured during the experiment is $\sim 26 \pm 1\,^{\circ}\mathrm{C}$ with low fluctuations. A detailed summary of environmental conditions during water condensation on Hsin film for various surfaces is presented in Table S1 of the Supplemental Material [40]. Since, during the experiment, no external humidifier or vapor generator is used, humidity and room temperatures are also not regulated, and the whole experiment is performed in one cycle without any delay or time interval between the experiments; also the condensation observed on Hsin film is purely from the water vapor present in the atmosphere.

APPENDIX C: IMAGE PROCESSING AND ANALYSIS OF THE IMAGES

The analysis of the captured images is performed by image processing approach using IMAGEJ software. The procedure involved in image processing and data extraction is detailed as shown in Fig. S4 [40]. The process starts with background noise cancellation for the original image [Fig. S4(a)]. The

background image [Fig. S4(b)] is obtained using a rolling ball approach with a radius of 50 pixels, and the subtracted image [Fig. S4(c)] is still a color image. The color image is first converted into grayscale image [Fig. S4(d)] and then to a binary image [Fig. S4(e)]. The lens effect of the droplets causes the center of droplets to appear as white pixels during binary conversion. All those are then filled with black pixels, using the fill-holes command [Fig. S4(f)], and each individual droplet is separated by single pixel spacing (only for those droplets which appear to be in contact), using the watershed command [Fig. S4(g)]. The specific Region of interest (ROI) is marked on the final frame (to avoid any possible aberration effect influencing the data analysis) of size 1000 × 600 pi ($595.95 \times 357.57\,\mu m^2$), with a specific coordinate (width = 1000, height = 600, X coordinate = 450, Y coordinate = 250; all values in pixels). The marked ROI is duplicated and analyzed. For a given ROI, an outline is drawn for every droplet along with the details, such as droplet count, area, positions (including X and Y coordinates), circularity, average size of all the droplets, and the total area covered by the droplets. The procedure is followed for all the frames with no changes, and for all the images captured while condensing water on Hsin-film surface. For images captured on glass surface, the rolling ball radius used during the background generation is increased up to 120, manually.

APPENDIX D: DROP SIZE DISTRIBUTION

In the histogram of drop count with respect to drop area (please see Sec. 6 in [40]), the bin width is set as $1\mu m^2$ with a bin limit of 0–2000 μm^2. When applied with voltage, the new generation of nucleated water drops is slightly inhibited. Compared to glass substrate, water drops on Hsin film are smaller in size but greater in count [Figs. S5(a) and S5(b) [40]]. Both Hsin film with voltage lower than threshold and glass substrate surfaces showed new cycles of condensation, causing bimodal size distribution [Figs. S5(a)–S5(c)]. The bimodal size distribution vanishes when applied with higher voltages since new nuclei are adsorbed more easily by the initial drops with lowered CAH and induced transportation [Figs. S5(d)–S5(g)].

APPENDIX E: NUCLEATION DENSITIES

According to classical nucleation theory, water condensation starts from heterogeneous nucleation of water molecules transform into nuclei on surface. The nucleation rate, count of nuclei formed per unit area per unit time, is theoretically presumed as

$$N_{\text{het}} \approx N_s \exp\left(-\frac{16\pi {\gamma_{LV}}^3}{3\Delta {G_v}^2 k_B T} S(\theta)\right), \tag{E1}$$

where γ_{LV} is the surface tension of water-air interface, ΔG_v is related to latent heat released for nucleation, K_B is the Boltzmann constant, and T is the temperature in K. $S(\theta) = (2 + \cos\theta)(1 - \cos\theta)^2/4$ is a geometrical factor accounting for the surface tension required when a drop forms on a surface, which is a function of contact angle θ. N_s is the nucleation site density, which is estimated by Rose as [52]

$$N_s = 0.037/r_{\text{min}}^2, \tag{E2}$$

where r_{min} is the smallest drop radius possible corresponding to the equilibrium in specified subcooling conditions. By inserting the parameters into Eq. (E2), the nucleation site density is found to be $\sim 1.67 \times 10^{11}/\text{cm}^2$. However, both theoretical and experimental studies reported nucleation site density of $\sim 10^6$–$10^8/\text{cm}^2$ [53,54]. This discrepancy might result from the different methods used in the evaluation.

The drop density is the measured count of drops divided by area of the region of interest (0.212 mm^2) and the evolution of drop density is shown in Fig. S6(a) [40]. Since the decay of drop density is the result of coalescence of the initial nuclei, we estimated the nuclei density at $t = 0$s by extrapolating the drop density as a function of time with exponential function $N = A \times \exp(-t/t) + N_0$. The results are shown in Fig. S6(b) [40]. On glass surface, the nuclei density is $5 \times 10^5/\text{cm}^2$ [black line in Fig. S6(b)]. In comparison with the literature, the nucleation density is reported to be in the order of 10^4–$10^6/\text{cm}^2$ [55]. The nuclei density was $\sim 1.7 \times 10^6/\text{cm}^2$ on Hsin film without applied voltage and decreased to $0.9 \times 10^6/\text{cm}^2$ when voltage of $200\,V_{\text{rms}}$ was applied [red dots in Fig. S6(b)]. According to Eq. (E1), despite that Hsin film has a higher contact angle than glass in the macroscopic scale, the heterogeneity and roughness of Hsin film provides four times more nucleation sites for water nucleation.

Here, we assumed the nucleation sites density is $10^7/\text{cm}^2$, and we applied the result of contact angle measurement on Hsin film to Eq. (E1) to obtain theoretical nuclei density with different applied voltage. The blue diamonds in Fig. S6(b) show that the theoretical nuclei density slightly increases with rising surface tension of Hsin film, which does not fit with our experimental result. When no voltage is applied, the nuclei density is approximately five times less than the theoretical estimation since the experiment is conducted in open space and air flow slightly disturbed the nucleation. With applied voltage, the nuclei density decreases rather than increasing according to theoretical estimation. We conjectured that other than contact angle, nucleation site density is another factor that might cause variation in nuclei density. Considering Hsin-film surface to be heterogeneous, nucleation site density according to the heterogeneity of the surface is estimated as

$$N_f = fN_s, \tag{E3}$$

where f is the area ratio of surface fraction with higher intrinsic surface tension to the entire heterogeneous surface. On Hsin film, when applied with voltage, the nucleation occurs on the LC domains rather than on polymer grains when no voltage is applied. This may be due to a change in thermal conductivity and surface tension when the LC reorientation takes place [56]. According to SEM image analysis, the LC domain occupied 31% of the surface. Hence, the factor f should be 0.69 when the voltage is lower than threshold, and it should be 0.31 when the voltage is higher than threshold. When substituting N_s in Eq. (E1) with N_f in Eq. (E3), the nuclei density of Hsin film is estimated to decrease by

$31/69 = 0.45$ compared with the nuclei density of 0 V, which is $\sim 0.8 \times 10^6/\text{cm}^2$ which is shown by the green dashed line in Fig. S6(b). The experimental result agrees with the estimation when the voltage is higher than $120\,V_{\text{rms}}$, indicating that the orientation of LCs controls the nucleation rate by tuning the location where nucleation occurs.

[1] M. M. Mekonnen and A. Y. Hoekstra, Four billion people facing severe water scarcity, Sci. Adv. **2**, e1500323 (2016).

[2] R. Tu and Y. Hwang, Reviews of atmospheric water harvesting technologies, Energy **201**, 117630 (2020).

[3] R. A. Sigsbee and G. M. Pound, Heterogeneous Nucleation from the Vapor, Adv. Colloid Interface Sci. **1**, 335 (1967).

[4] D. Beysens, The formation of dew, Atmos. Res. **39**, 215 (1995).

[5] D. Beysens, Dew nucleation and growth, C. R. Phys. **7**, 1082 (2006).

[6] B. ElFil, G. Kini, and S. Garimella, A review of dropwise condensation: Theory, modeling, experiments, and applications, Int. J. Heat Mass Transfer **160**, 120172 (2020).

[7] Y. Tu, R. Wang, Y. Zhang, and J. Wang, Progress and expectation of atmospheric water harvesting, Joule **2**, 1452 (2018).

[8] K. Rykaczewski, A. T. Paxson, M. Staymates, M. L. Walker, X. Sun, S. Anand, S. Srinivasan, G. H. McKinley, J. Chinn, and J. H. J. Scott, Dropwise condensation of low surface tension fluids on omniphobic surfaces, Sci. Rep. **4**, 4158 (2014).

[9] J. W. Rose, Dropwise condensation theory and experiment: A review, Proc. Inst. Mech. Eng., Part A **216**, 115 (2002).

[10] X. Liu and P. Cheng, Dropwise condensation theory revisited: Part I. droplet nucleation radius, Int. J. Heat Mass Transfer **83**, 833 (2015).

[11] X. Liu and P. Cheng, Dropwise condensation theory revisited Part II. droplet nucleation density and condensation heat flux, Int. J. Heat Mass Transfer **83**, 842 (2015).

[12] T. R. Linderoth, V. P. Zhdanov, and B. Kasemo, Water Condensation Kinetics on a Hydrophobic Surface, Phys. Rev. Lett. **90**, 156103 (2003).

[13] A. Menchaca-Rocha, A. Martínez-Dávalos, R. Nunez, S. Popinet, and S. Zaleski, Coalescence of liquid drops by surface tension, Phys. Rev. E **63**, 046309 (2001).

[14] H. Zhao and D. Beysens, From droplet growth to film growth on a heterogeneous surface: Condensation associated with a wettability gradient, Langmuir **11**, 627 (1995).

[15] C. S. Sharma, C. Stamatopoulos, R. Suter, P. R. vonRohr, and D. Poulikakos, Rationally 3D-textured copper surfaces for laplace pressure imbalance-induced enhancement in dropwise condensation, ACS Appl. Mater. Interfaces **10**, 29127 (2018).

[16] H. Cha, H. Vahabi, S. Chavan, A. Wu, M.-K. Kim, S. Sett, S. A. Bosch, W. Wang, A. K. Kota, and N. Miljkovic, Dropwise condensation on solid hydrophilic surfaces, Sci. Adv. **6**, eaax0746 (2020).

[17] A. R. Parker and C. R. Lawrence, Water capture by a desert beetle, Nature (London) **414**, 33 (2001).

[18] K. K. Varanasi, M. Hsu, N. Bhate, W. Yang, and T. Deng, Spatial control in the heterogeneous nucleation of water, Appl. Phys. Lett. **95**, 94101 (2009).

[19] Y. Lu, L. Yu, Z. Zhang, S. Wu, G. Li, P. Wu, Y. Hu, J. Li, J. Chu, and D. Wu, Biomimetic surfaces with anisotropic sliding wetting by energy-modulation femtosecond laser irradiation for enhanced water collection, RSC Adv. **7**, 11170 (2017).

[20] P.-B. Bintein, H. Lhuissier, A. Mongruel, L. Royon, and D. Beysens, Grooves Accelerate Dew Shedding, Phys. Rev. Lett. **122**, 098005 (2019).

[21] R. Enright, N. Miljkovic, J. L. Alvarado, K. Kim, and J. W. Rose, Dropwise condensation on micro-and nanostructured surfaces, Nanoscale Microscale Thermophys. Eng. **18**, 223 (2014).

[22] P. Kim, T. -S. Wong, J. Alvarenga, M. J. Kreder, W. E. Adorno-Martinez, and J. Aizenberg, Liquid-infused nanostructured surfaces with extreme anti-ice and anti-frost performance, ACS Nano **6**, 6569 (2012).

[23] X. Dai, N. Sun, S. O. Nielsen, B. B. Stogin, J. Wang, S. Yang, and T. -S. Wong, Hydrophilic directional slippery rough surfaces for water harvesting, Sci. Adv. **4**, eaaq0919 (2018).

[24] P. B. Weisensee, Y. Wang, H. Qian, D. Schultz, W. P. King, and N. Miljkovic, Condensate droplet size distribution on lubricant-infused surfaces, Int. J. Heat Mass Transfer **109**, 187 (2017).

[25] K. Li, J. Ju, Z. Xue, J. Ma, L. Feng, S. Gao, and L. Jiang, Structured cone arrays for continuous and effective collection of micron-sized oil droplets from water, Nat. Commun. **4**, 2276 (2013).

[26] Y. Zheng, H. Bai, Z. Huang, X. Tian, F.-Q. Nie, Y. Zhao, J. Zhai, and L. Jiang, Directional water collection on wetted spider silk, Nature (London) **463**, 640 (2010).

[27] K.-C. Park, P. Kim, A. Grinthal, N. He, D. Fox, J. C. Weaver, and J. Aizenberg, Condensation on slippery asymmetric bumps, Nature (London) **531**, 78 (2016).

[28] S. Khandekar and K. Muralidhar, *Dropwise Condensation on Inclined Textured Surfaces* (Springer, New York, 2014).

[29] K. B. Jinesh and J. W. M. Frenken, Capillary Condensation in Atomic Scale Friction: How Water Acts like a Glue, Phys. Rev. Lett. **96**, 166103 (2006).

[30] N. Verplanck, Y. Coffinier, V. Thomy, and R. Boukherroub, Wettability switching techniques on superhydrophobic surfaces, Nanoscale Res. Lett. **2**, 577 (2007).

[31] K. Ichimura, S.-K. Oh, and M. Nakagawa, Light-driven motion of liquids on a photoresponsive surface, Science **288**, 1624 (2000).

[32] D. Baratian, R. Dey, H. Hoek, D. van denEnde, and F. Mugele, Breath Figures under Electrowetting: Electrically Controlled Evolution of Drop Condensation Patterns, Phys. Rev. Lett. **120**, 214502 (2018).

[33] R. Dey, J. Gilbers, D. Baratian, H. Hoek, D. van denEnde, and F. Mugele, Controlling shedding characteristics of condensate drops using electrowetting, Appl. Phys. Lett. **113**, 243703 (2018).

[34] Y. Jin, L. Zhang, and P. Wang, Atmospheric water harvesting: Role of surface wettability and edge effect, Glob. Challenges **1**, 1700019 (2017).

[35] P. M. Winkler, A. Vrtala, P. E. Wagner, M. Kulmala, K. E. J. Lehtinen, and T. Vesala, Mass and Thermal Accommodation

during Gas-Liquid Condensation of Water, Phys. Rev. Lett. **93**, 075701 (2004).

[36] Y.-P. Chiu, C.-Y. Shen, W.-C. Wang, T.-Y. Chu, and Y.-H. Lin, Electrically surface-driven switchable wettability of liquid crystal/polymer composite film, Appl. Phys. Lett. **96**, 131902 (2010).

[37] Y.-H. Lin, T.-Y. Chu, Y.-S. Tsou, K.-H. Chang, and Y.-P. Chiu, An electrically switchable surface free energy on a liquid crystal and polymer composite film, Appl. Phys. Lett. **101**, 233502 (2012).

[38] J. D. Parsons, A Molecular theory of surface tension in nematic liquid crystals, J. Phys. **37**, 1187 (1976).

[39] P. Hubert and Y. Galerne, Surface tensions and anchoring transitions of nematic liquid crystals on gradually oxidized substrates, Appl. Phys. Lett. **71**, 1050 (1997).

[40] See Supplemental Material at http://link.aps.org/supplemental/10.1103/PhysRevE.104.034701 for detailed experimental results.

[41] E. Chibowski, Surface free energy of a solid from contact angle hysteresis, Adv. Colloid Interface Sci. **103**, 149 (2003).

[42] D. Fritter, C. M. Knobler, D. Roux, and D. Beysens, Computer simulations of the growth of breath figures, J. Stat. Phys. **52**, 1447 (1988).

[43] F. Family and P. Meakin, Kinetics of droplet growth processes: Simulations, theory, and experiments, Phys. Rev. A **40**, 3836 (1989).

[44] H. Azarinia, J. Beeckman, K. Neyts, E. Schacht, J. Gironès, R. James, and F. A. Fernandez, Orientation of nematic liquid crystal in open glass microstructures, J. Appl. Phys. **106**, 63101 (2009).

[45] H. Bai, X. Tian, Y. Zheng, J. Ju, Y. Zhao, and L. Jiang, Direction controlled driving of tiny water drops on bioinspired artificial spider silks, Adv. Mater. **22**, 5521 (2010).

[46] T. M. Rogers, K. R. Elder, and R. C. Desai, Droplet growth and coarsening during heterogeneous vapor condensation, Phys. Rev. A **38**, 5303 (1988).

[47] A. Steyer, P. Guenoun, D. Beysens, and C. M. Knobler, Growth of droplets on a substrate by diffusion and coalescence, Phys. Rev. A **44**, 8271 (1991).

[48] P. Meakin, Droplet deposition growth and coalescence, Rep. Prog. Phys. **55**, 157 (1992).

[49] D. Beysens and C. M. Knobler, Growth of Breath Figures, Phys. Rev. Lett. **57**, 1433 (1986).

[50] E. L. Hinrichsen, J. Feder, and T. Jøssang, Geometry of random sequential adsorption, J. Stat. Phys. **44**, 793 (1986).

[51] U. Delabre, C. Richard, and A. M. Cazabat, Some specificities of wetting by cyanobiphenyl liquid crystals, J. Phys.: Condens. Matter **21**, 464129 (2009).

[52] J. W. Rose, Further aspects of dropwise condensation theory, Int. J. Heat Mass Transfer **19**, 1363 (1976).

[53] C. Graham, and P. Griffith, Drop size distributions and heat transfer in dropwise condensation, Int. J. Heat Mass Transfer **16**, 337 (1973).

[54] H. W. Wen and R. M. Jer, On the heat transfer in dropwise condensation, Chem. Eng. J. **12**, 225 (1976).

[55] R. N. Leach, F. Stevens, S. C. Langford, and J. T. Dickinson, Dropwise condensation: Experiments and simulations of nucleation and growth of water drops in a cooling system, Langmuir **22**, 8864 (2006).

[56] J. Shin, M. Kang, T. Tsai, C. Leal, P. VBraun, and D. G. Cahill, Thermally functional liquid crystal networks by magnetic field driven molecular orientation, ACS Macro Lett. **5**, 955 (2016).